Propagation Analysis of the 3rd Sonic Boom Prediction Workshop Cases using sBOOM

Sriram K. Rallabhandi*
NASA Langley Research Center, Hampton, VA, 23681

The 3rd Sonic Boom Prediction Workshop was held on January 4-5, 2020 in conjunction with the AIAA SciTech conference. The workshop had 23 participants who represented 6 different countries and 18 unique organizations that included government, industry, and academia. The workshop was attended by over 50 individuals. The motivation for the workshop stems from the goal of obtaining supersonic commercial overland flight. In order to replace the current prohibition with a certification standard, an international effort is required to quantify the accuracy and reliability of prediction methods. The workshops also identify deficiencies in existing methods where further research should be focused. The workshop consisted of two days with the first day focused on near-field computational fluid dynamics (CFD) and the second day on propagation techniques. For the atmospheric propagation portion of the workshop, two required cases and one optional case were prescribed for the participants to exercise their propagation implementations. This paper presents and discusses the results that were obtained using the sonic boom propagation code sBOOM. Results show that sonic boom carpets could be much different under arbitrary atmospheric conditions as opposed to standard atmospheric conditions. Additionally, several unique features when using sBOOM are presented.

I. Nomenclature

$ASEL$	=	A-weighted Sound Exposure Level (decibels)
B	=	Blokhintzev Invariant
$BSEL$	=	B-weighted Sound Exposure Level (decibels)
c	=	Speed of sound
$CSEL$	=	C-weighted Sound Exposure Level (decibels)
D	=	Doppler Shift induced by prevailing winds
f_{ac}	=	Characteristic acoustic frequency of the incoming waveform
$LNTE$	=	Lossy Nonlinear Tricomi Equation
m_ν	=	Relaxation
OML	=	Outer Mold Line of the underlying aircraft concept
P	=	Pressure variable
PHI	=	Azimuthal angle for atmospheric propagation
PL	=	Perceived Level of outdoor sonic booms (decibels)
$\vec{q}$	=	Slowness vector
t_ν	=	Relaxation time
v_g	=	Magnitude of ray velocity
R_{cau}	=	Radius of curvature of the caustic surface
R_{ray}	=	Radius of curvature of the caustic ray
R_{tot}	=	Relative radius of curvature
S	=	Ray-tube area
t	=	Time step during propagation
$\vec{w}$	=	Wind velocity vector
$\overline{Z}$	=	Non-dimensional parameter of the focal region computational domain
β	=	Non-dimensional nonlinear parameter in the Augmented Burgers Equation (1.2)
δ	=	Diffraction boundary layer thickness

*Aerospace Engineer, Aeronautics Systems Analysis Branch, Mail Stop 442, and AIAA Associate Fellow

$\hat{n}$ = Unit vector normal to the wavefront
Ω = 1/D
ρ = Density
σ = Non-dimensional step size along the propagation direction
τ = Discretization variable of the underlying pressure waveform

II. Introduction

The 3rd Sonic Boom Prediction Workshop was held on January 4-5, 2020 in conjunction with the AIAA SciTech 2020 conference. Similar to the earlier boom prediction workshops [1–3], the first day consisted of near-field Computational Fluid Dynamics (CFD) predictions whereas the second day concentrated on atmospheric propagation predictions of the ground signatures, loudness metrics, and extent of sonic boom primary carpets. This paper provides a discussion of the cases as analyzed using an augmented Burgers solver, sBOOM. Although the underlying mechanisms of the propagation modeling haven't changed since the original publication of sBOOM [4], there have been several enhancements, bug fixes, and improvements over the years. After this introductory section, the paper is divided as follows. Section III briefly describes the augmented Burgers equation used within sBOOM along with ray path equations. Section IV discusses the cases used in the workshop. Section V delves into the numerical results obtained for each of the cases along with detailed discussion of the ground signatures and observations related to them. Finally, section VI summarizes the work and provides appropriate conclusions.

III. Ray Acoustics, Burgers Equation and Solution Approach

Sonic boom predictions within sBOOM are split into two independent portions, a) ray path calculation, which includes wind effects, aging, and ray-tube area computation, and b) numerical implementation of the wave propagation along these ray paths until the disturbance reaches the ground. The following sections briefly describe these mechanisms.

A. Ray Paths

The ray path equations used are coupled differential equations [5, 6] listed in Eqs. (1) and (2). In these equations, t is the propagation time along a ray. Other relevant parameters are defined as given in Eq. (3). In these equations, c is the speed of sound, $\overline{w}$ is the wind speed vector, ρ is the atmospheric density, $\vec{q}$ is the slowness vector, D is the Doppler shift induced by the prevailing winds and B is a manifestation of the conservation of energy along ray tubes (similar to stream tubes in fluid flow) called the Blokhintzev invariant. The coupled equations are solved to second-order accuracy to determine ray paths. The ray-tube area is calculated from four rays that are azimuthally and temporally separated. Using four rays to determine ray-tube areas poses certain difficulties which are exacerbated in cases and atmospheres where temperature and wind gradients are strong. Methods exist in literature [7] where ray-tube areas are computed using a single ray by differentiating the ray path equations with respect to the azimuthal angle and time of emission from the vehicle. Work presented here computes ray-tube areas using four rays; however, future work may include ray path Jacobians to compute ray-tube areas.

$$\frac{d\vec{x}}{dt} = \vec{w} + c^2\vec{q}D \tag{1}$$

$$\frac{d\vec{q}}{dt} = -\left[\frac{\nabla c}{cD} + \sum_{i=1}^{3} q_i \nabla w_i\right] \tag{2}$$

$$\begin{aligned} \vec{q} &= \tfrac{\hat{n}}{c+\vec{w}.\hat{n}} \\ D &= 1 + \tfrac{\vec{w}.\hat{n}}{c} \\ \vec{v_g} &= c\hat{n} + \vec{w} \\ B &= \sqrt{\frac{\rho c S_0 D_0^2}{\rho_0 c_0 S D^2}\frac{\frac{cv_{g,0}}{D_0}}{\frac{c_0 v_g}{D}}} \end{aligned} \tag{3}$$

B. Burgers Equation and Numerical Solution

sBOOM [4] uses a lossy Burgers equation model as given in Eq. (4) to numerically model the sonic boom propagation physics. Detailed derivations and the underlying assumptions related to this are provided in earlier publications [8–10] based on approximations to the Westervelt Equation using weakly nonlinear ray theory. Because there are no closed-form solutions to this equation, it is solved numerically using a split-step approach [11] where each term on the right-hand side is separated and solved independently under the assumption that the cumulative errors are small if the step size is small. The step size itself it determined dynamically within the algorithm to ensure that the underlying waveform does not become multi-valued. These approaches are documented in earlier work [10] and are not described in detail here. Each of the individual mechanisms (nonlinearity, thermo-viscous absorption, molecular relaxation, atmospheric stratification and ray-tube spreading) is solved in the time domain. Although absorption and relaxation are numerically solved using second-order finite difference approximations, nonlinearity is solved using the Poisson solution [10] on the distorted grid with re-interpolation back to the original uniform mesh. Additional details are provided in past publications [4, 12].

$$\frac{\partial P}{\partial \sigma} = \frac{\frac{\partial B}{\partial \sigma}}{B} P + \frac{\beta \Omega}{2\rho_0 c_0^3} \left(\frac{c_0}{v_g}\right) \frac{\partial P^2}{\partial \tau} + \frac{\delta \Omega^2}{2\rho_0 c_0^3} \left(\frac{c_0}{v_g}\right) + \frac{\partial^2 P}{\partial \tau^2} + \Sigma_\nu \frac{m_\nu}{2c_0} \frac{t_\nu \Omega^2}{1 + t_\nu \Omega \frac{\partial}{\partial \tau}} \left(\frac{c_0}{v_g}\right) \frac{\partial^2 P}{\partial \tau^2} \tag{4}$$

In addition to propagating the waveforms through the atmosphere, sBOOM also computes multiple loudness metrics ($ASEL$, $BSEL$, $CSEL$, and PL) using robust digital filters. The Mark VII Perceived Level (PL) of Stevens [13] is adopted as a measure to compare workshop submissions because it is correlated with loudness and annoyance in multiple experiments. [14, 15]. Additional metrics are calculated to investigate how they behave with respect to the perceived level. These other metrics have been shown to correlate well with multiple laboratory datasets of human annoyance to sonic booms in both outdoor and indoor environments [15].

IV. Cases for Propagation

A. Case 1: C25P

The propagation portion of the workshop included two required cases where cruise boom is predicted and an optional case for simulating boom focusing. The concept investigated as Case 1 in SBPW3 is shown in Fig. 1(a) and the off-body pressure waveform (often referred to as the *near-field pressure waveform*) corresponding to this concept is shown in Fig. 1(b). For the sake of de-cluttering, data corresponding to only some selected azimuthal angles are shown; however, CFD near-field data were provided at azimuthal angles ranging from −90° to 90° in 10° increments. It is important to note that from the point of view of the pilot, positive azimuths are defined as being to his/her right and negative azimuths are to his/her left. For the wind convention, the positive X-wind is a tailwind if the aircraft is flying east, as is the case for all the simulations in this work. Positive Y-wind is going north, i.e., from a pilot's point of view, positive Y-wind is blowing toward his/her left. Put another way, if an aircraft were flying north, positive Y-wind is a tailwind. The near-field data were generated at cruise conditions of M=1.4 and an altitude of 51,706 ft.

(a) **NASA Concept C25P**

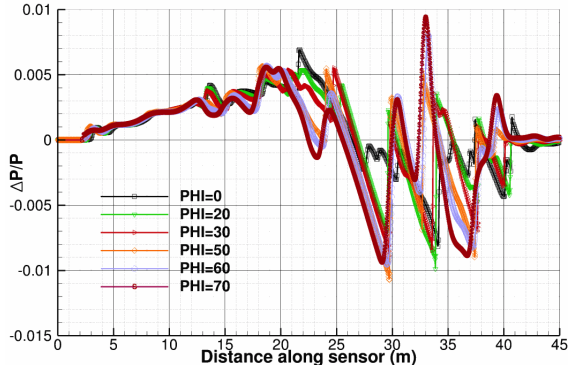

(b) **C25P near-field pressures**

Fig. 1 Case 1: C25P.

For this concept, an optional case was also requested where level acceleration flight conditions are simulated.

Acceleration and other maneuvers usually lead to higher sonic boom loudness levels due to what is termed as transient focused booms. These are discussed in more detail in Section V.B

B. Case 2: C609

The second case used in the workshop is a variant of the X-59 Low Boom Flight Demonstrator (LBFD) [16] aircraft referred to as C609 by the contractor team and NASA. The Lockheed Martin Corporation (LM) has been awarded a contract to manufacture the X-59 to demonstrate unique boom shaping technologies and address system integration challenges associated with limiting maximum sonic boom Perceived Level (PL) of loudness to less than 75 dB across the entire carpet while flying at a Mach number of 1.4 and an altitude of 54,000 ft. Initial flights of the X-59 are expected to begin in the 2021-2022 time frame, with validation runs and community tests expected at multiple locations following envelope expansion flights. Figure 2(a) depicts a rendering of the concept used in this study, and Fig. 2(b) shows the near-field pressure waveforms at selected azimuthal angles. Even though only a few selected angles are shown, detailed CFD off-body pressures were provided at every 2° degrees from -90° to 90°.

(a) **Low Boom Flight Demonstrator Variant C609**

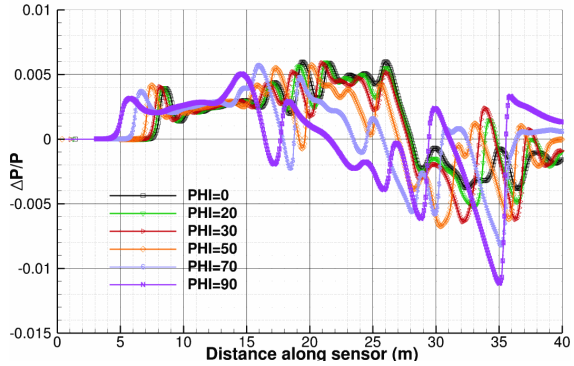

(b) **C609 near-field pressures**

Fig. 2 Case 2: C609.

The propagation simulations were required using prescribed non-standard atmospheric conditions. The idea was to rigorously test the ray path integration and implementation of the underlying physical mechanisms under realistic windy conditions. Additional details on the cases, flight conditions, and atmospheric conditions are given in the 3rd Sonic Boom Prediction Workshop (SBPW3) propagation summary paper [17].

V. Results and Discussion

The details of the 3^{rd} sonic boom propagation cases as simulated using sBOOM are presented in this section. Discussion of the results is provided where appropriate. Certain unique features and observations are provided as well.

A. Case 1: C25P

The given near-fields are propagated to the ground to first determine lateral cut-off azimuthal angles, which turn out to be -78.3° and 69.1°. These angles are much larger than those under standard atmospheric conditions, which for reference are $\pm 50.8^\circ$. This translates to an increase in primary carpet width of about 15.38 nautical miles for positive azimuthal angles and about 29.95 nautical miles for negative azimuthal angles compared to the standard atmospheric conditions. Figure 3 depicts the ground signatures computed at some selected azimuthal angles. The primary observations from this plot are:

1) Ground signatures along the flight track (azimuthal angle of 0) have the highest pressure rise magnitudes and these gradually decrease as the azimuthal angle magnitude increases on either side.
2) Even though the near-field pressures are symmetric around the aircraft, the ground signatures are asymmetric due to the directivity of the prevailing winds.
3) Signatures near lateral-cutoff angles are quite small in amplitude. This is due to the long distances associated with these edge-of-the-carpet rays, which in turn attenuates the signal significantly.

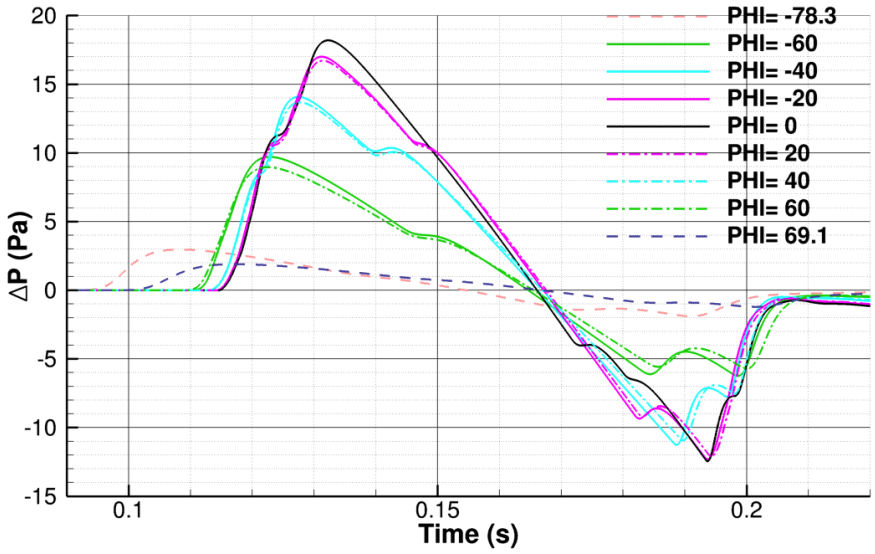

Fig. 3 Case 1 ground signatures.

Figure 4 shows the loudness carpet for Case 1. Four different loudness metrics, Perceived Level (PL), A-weighted Sound Exposure Level (ASEL), B-weighted Sound Exposure Level (BSEL), and C-weighted Sound Exposure Level (CSEL), are plotted. All the loudness metrics are highly correlated across the primary boom carpet. PL and BSEL are quite close to each other across most of the carpet; PL drops sharply compared to BSEL towards the edge of the carpet.

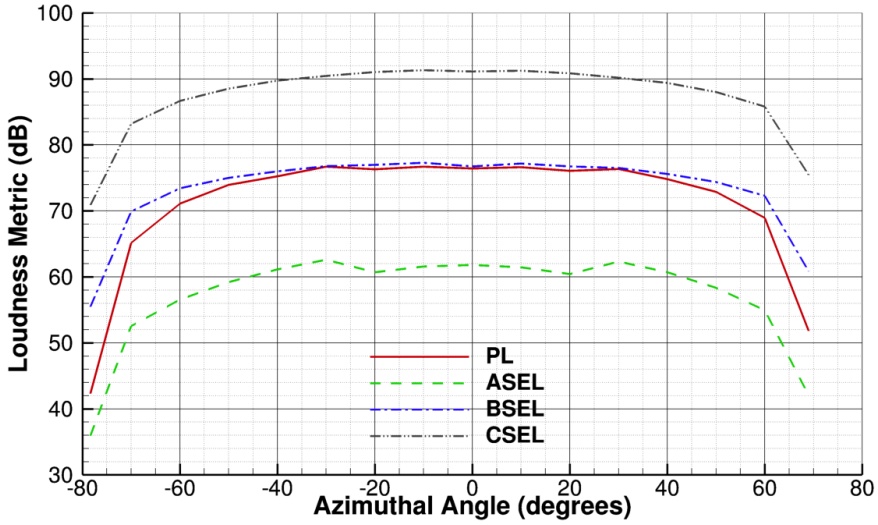

Fig. 4 Case 1 sonic boom loudness carpet.

B. Optional Focus Case: C25P

This section provides details regarding the computations needed to predict the focus boom signatures corresponding to the optional level acceleration case. This work heavily leverages the Lossy Nonlinear Tricomi Equation (LNTE) solver developed as part of the NASA's Superboom Caustic Analysis and Measurement Program (SCAMP) [18]. It has been shown that the LNTE solver predictions agreed well with experimental data.

The following description will discuss the detailed interface between the Burgers solver within sBOOM and LNTE to be able to correctly predict the focus, post-focus, and evanescent waves. Detailed discussion of this interface has been covered in earlier literature [19–21]. Figure 5 shows the underlying process to determine the data hand-off between the

two codes. The caustic line or surface is computed by moving back and forth from the given flight conditions along the flight trajectory and determining the focal points. The locus of the focal points is termed as the caustic line or surface. Geometric ray acoustic theory breaks down in regions around this caustic surface. To overcome this shortcoming, the nonlinear Tricomi equation was developed. The discussion below is to set up the computational domain around the caustic surface to predict ground signatures corresponding to the area around the caustic surface a) behind (also called evanescent waves), b) on (focus booms), and c) ahead (post-focus booms) where reflections off the caustic surface are captured.

The first step in setting up the computational domain for the LNTE is to compute the intersection of the caustic surface with the ground (see Fig. 5). The caustic tangent ray is then determined as the ray from the vehicle that intersects the ground at the same point as the intersection of the caustic line with the ground. The radius of curvature of the caustic line (R_{cau}) and the radius of curvature of the caustic tangent ray (R_{ray}) are determined. From these values, the total radius of curvature is calculated as $\frac{1}{R_{tot}} = \frac{1}{R_{cau}} - \frac{1}{R_{ray}}$. In the current case, R_{cau} was computed to be $\approx 57,921$ meters, and R_{ray} was computed as $\approx 108,040$ meters resulting in R_{tot} being $\approx 124,859$ meters. The characteristic frequency (f_{ac}), which is equal to the frequency corresponding to the maximum power spectrum of the incoming waveform, is computed to be 7.42 Hz. Based on the computational domain of the LNTE solver, the non-dimensional coordinate $\overline{Z}$ is the ratio of the normal distance from the caustic line intersection with the ground (Z) to the diffraction boundary layer thickness (Eq. (5)). When $\overline{Z} = 1$, the normal distance would simply be the diffraction boundary layer thickness, which is computed as $\left[\frac{2f_{ac}^2}{R_{tot}c_0^2}\right]^{-1/3}$. Based on the computed characteristic frequency and total radius of curvature, the diffraction boundary layer thickness was computed to be 506.8 meters. After initial comparison of results from the workshop participants, it was discovered that the values computed for the characteristic frequencies and caustic geometries varied, leading to differences in the diffraction boundary layer thickness values and therefore the computation of the delta ray. The participants were subsequently asked to calculate boom signatures around the caustic with a prescribed boundary layer thickness (δ) of 302.4 meters to enable consistent computations for comparison.

$$\overline{Z} = Z\left[\frac{2f_{ac}^2}{R_{tot}c_0^2}\right]^{1/3} \tag{5}$$

The determination of the delta ray begins with the computation of the point in space δ normal distance away from the caustic line intersection with the ground. This point (say S) is labeled as the interface point between Burgers and LNTE solvers. The flight conditions when the caustic ray intersects the ground are Mach = 1.4121, Altitude = 45,000 ft, an acceleration of $\frac{dM}{dt} = 0.015681$, and a rate of change of acceleration of $\frac{d^2M}{dt^2} = 0.000359$. Assuming the time along flight trajectory at the caustic tangent ray flight conditions to be 0 (refers to the point labeled "Given (M,$\frac{dM}{dt}$,$\frac{d^2M}{dt^2}$)" in Fig. 5), time is advanced incrementally to determine the flight time that makes the corresponding ray, named the delta ray, to pass through S. For this case, the time advance is 6.44 seconds beyond the caustic ray flight conditions and the updated flight conditions are $M = 1.5206$, $\frac{dM}{dt} = 0.017996$. This point is the origination of the delta ray path and is labeled as "New (M,$\frac{dM}{dt}$,$\frac{d^2M}{dt^2}$)" in Fig. 5.

Burgers propagation is carried out starting from the origination of the delta ray path until an altitude that corresponds to the location that is labeled as the "Interface point between Burgers and LNTE" and the resulting waveform at this location, without the ground reflection factor, is termed as the "incoming waveform." This is then used as the incoming ray input to the LNTE solver to determine the focus (and post-focus) signatures corresponding to the caustic ray conditions. It is a little counter-intuitive to perform Burgers analysis on the delta ray to be able to compute the focus boom signature corresponding to the caustic ray conditions. If one were to ignore the delta ray computation procedure and use the caustic ray conditions to determine the incoming waveform input to LNTE, the results could be significantly different. As a comparison, Fig. 6 depicts the incoming waveform that is computed on the delta ray along with that computed on the caustic ray. When propagating on the caustic ray, the pressures are scaled up due to the Blokhintzev invariant as the ray-tube area decreases due to its proximity to the caustic surface and the focal point. The waveforms shown here do not include the ground reflection factor.

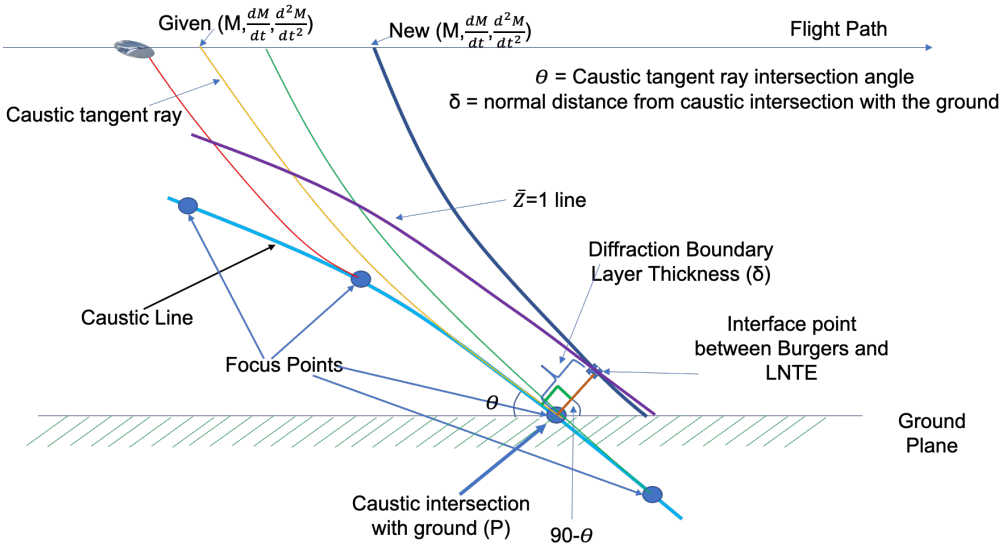

Fig. 5 Focusing geometry during level acceleration.

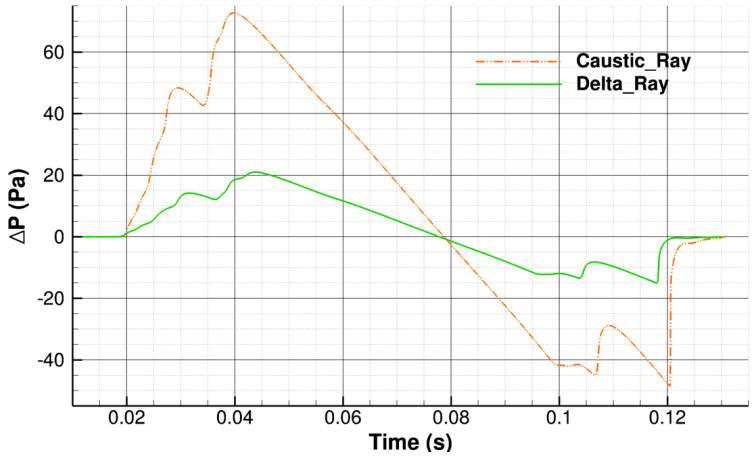

Fig. 6 Waveforms computed from Burgers at the interface with the LNTE domain.

Even though the caustic geometry computations result in a deterministic value for R_{tot}, the value of δ was fixed for the workshop case. Since R_{tot} is dependent on f_{ac}, and δ, it cannot be varied independently. Hence, in this work, a R_{tot} value of $\approx 26,532$ meters, computed based on the prescribed value of δ and a f_{ac} value of ≈ 7.42 Hz, is used instead of the value computed based on the caustic geometry. As has been mentioned previously, this was done to ensure all participants were consistent in the prediction of the delta ray conditions. Using the delta ray waveform as the input, the LNTE [22] solver was run over a computational domain of $\overline{Z} = [-1, 1]$. Figure 7 depicts the ground signatures, after applying a ground reflection factor of 1.9, at the requested $\overline{Z}$ locations. In addition, since the computational domain of LNTE is hyperbolic in the illuminated region ($\overline{Z} > 0$) and elliptic in the shadow zone ($\overline{Z} < 0$), the computational solution procedure involves numerical marching through the waveforms from the incoming to the outgoing profiles. Just like the Burgers solver, the LNTE solution process involves using the splitting method to separate the effects of diffraction, nonlinearity, absorption, and dispersion, while iteratively evolving in the non-dimensional time. Thus, when numerical convergence is achieved, solutions simultaneously exist at all discretized $\overline{Z}$ locations within the computational domain; however, only four waveforms are shown corresponding to the non-dimensional locations requested for the workshop. The following observations can be made concerning this figure:

1) In the shadow zone, the evanescent waves have much lower pressure magnitude compared to the pressures in the illuminated zone.

2) Maximum perceived level of loudness is achieved at a location slightly displaced from the focus location on the illuminated side at a $\overline{Z} = 0.05$. Ground signatures at this location are plotted as well for the sake of comparison.
3) The pressure waveform computed at the edge of the computational domain ($\overline{Z} = 1$) on the outgoing ray is comprised of a concatenation of two waves, the incoming waveform and a reflected waveform. As the distance from the caustic surface increases, the waveform reflected off the caustic dissipates, eventually resulting in a single waveform rather than a combination or concatenation of the two waves.
4) The perceived levels of loudness on the illuminated side in the small region around the caustic surface are much higher than the cruise boom levels, which are computed to be around 75 PLdB as seen in Fig. 4.

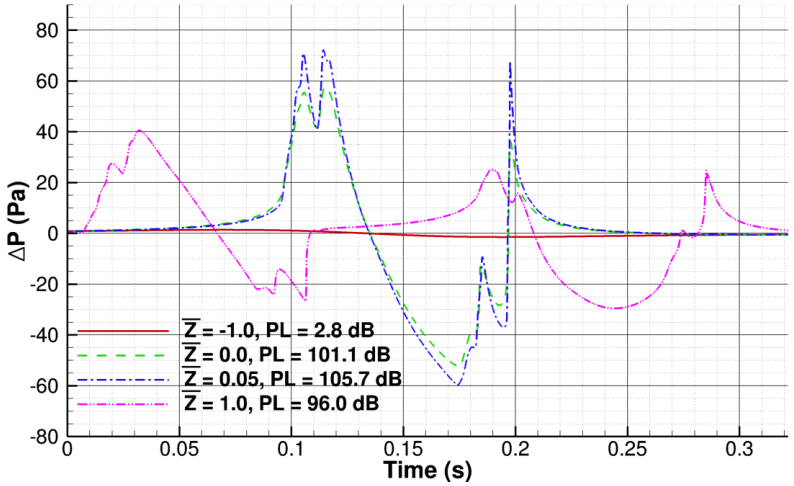

Fig. 7 Evanescent, focus, and post-focus ground signatures.

Figure 8 shows the iterative convergence history of the LNTE solution process as the pressure field evolves in pseudo-time. The computational domain is scanned to determine the largest pressure difference during each step normalized by the pseudo-time. It is seen that the convergence parameters reduce by six to eight orders of magnitude after a pseudo-time value of 20, showing that the results are sufficiently converged. Also plotted is the pseudo-time increment as the numerical solution evolves, which is a convergence parameter in itself. The pseudo-time increment value is proportional to the largest slope of the pressure field within the computational domain. Since this increment converges to a value, this indicates that the largest slope in the pressure field does not change much, which in turn indicates convergence in the pressure field evolution.

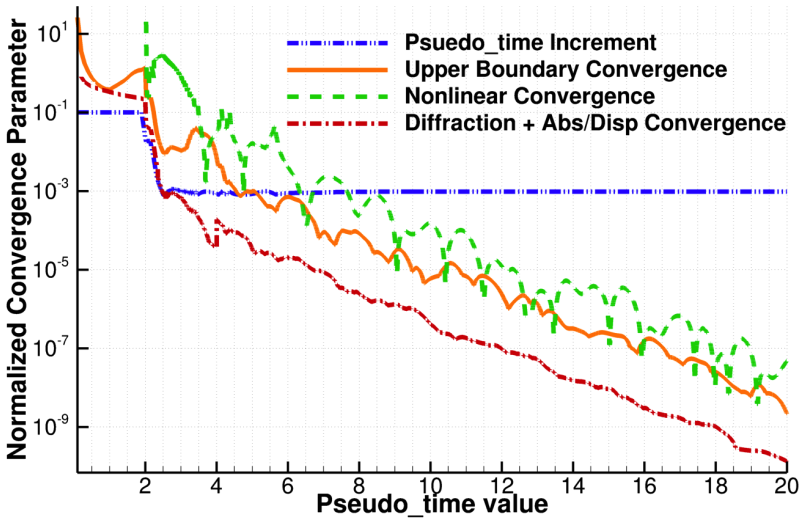

Fig. 8 Convergence history of the LNTE.

1. Sensitivity of Focus Signatures to R_{tot} and f_{ac}

Examining the nonlinear Tricomi equation being modeled in the LNTE numerical scheme [22], R_{tot} and f_{ac} feature prominently as the coefficients weighing the nonlinear and diffraction effects. This section provides details on the sensitivity of the LNTE solutions to the specification of either of those parameters. At lower Mach numbers, the rays emanating from the aircraft are steeper and the radius of curvature, R_{ray}, is much larger allowing the approximation $R_{tot} \approx R_{cau}$. Although that is not the case here, the following discussion makes this assumption to see the effect of approximating $R_{tot} \approx R_{cau} \approx 57,921$ meters as computed from the caustic geometry. The diffraction boundary layer distance in this case is computed to be 392.38 meters, and following the procedure described earlier, the corresponding delta ray conditions are computed to be $M = 1.5369$, $\frac{dM}{dt} = 0.018318$. Under these circumstances, to be consistent the ground signatures should be compared at a $\overline{Z}$ value of $302.4/392.38 = 0.7707$ to ensure that the physical locations where the signatures are compared are consistent. Secondly, characteristic frequency has also been defined [19] as the reciprocal of the characteristic duration T_{ac} of the incoming acoustical waveform. Although defining and obtaining T_{ac} is straightforward for N waves, it is much more involved when shaped sonic booms are concerned, especially because the pressures return to ambient conditions very slowly and gradually. One could determine T_{ac} by assuming the primary content of the sonic boom ground signature is within pressure energy/impulse values ranging from 99.9999% to 100% of the complete waveform. Using these settings, f_{ac} has a value between 7.63 Hz and 8.95 Hz for the focusing case being discussed in this paper. For the sake of comparisons here, we use a value of 8.95 Hz, which is farthest from the value computed using the power spectrum (7.42 Hz). In this case, the R_{tot} value is computed to ensure that the physical location at $\overline{Z} = 1$ aligns with the other cases. Table 1 provides the calculated values corresponding to these cases.

Table 1 Parameters for R_{tot} and f_{ac} Sensitivity Cases

Case	R_{tot} (m)	f_{ac} Hz	δ (m)	$\overline{Z}$ for same physical location
Baseline	26,532	7.42	302.4	1.0
R_{tot} Sensitivity	57,921	7.42	392.38	0.7707
f_{ac} Sensitivity	38,509	8.95	302.4	1.0

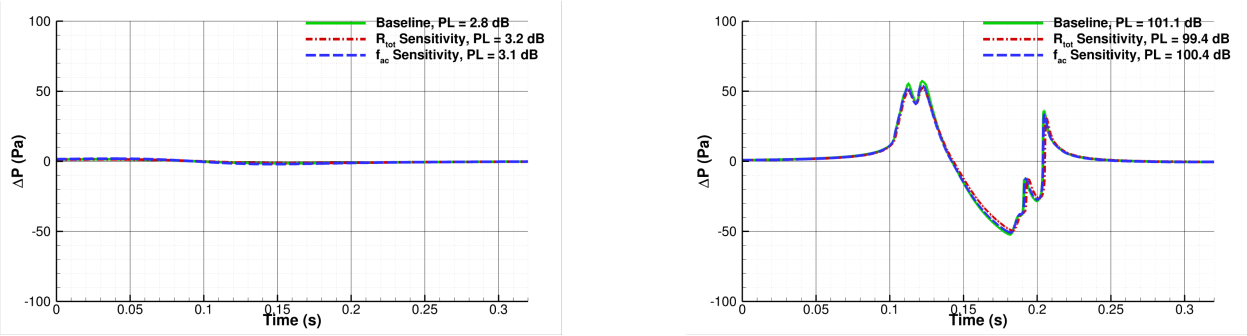

(a) $\overline{Z}$ = **-1.0** (b) $\overline{Z}$ = **0.0**

Fig. 9 Evanescent and focus ground signature sensitivity at azimuthal angle = 0°.

Figures 9-10 depict the evanescent, focus, and post focus ground signatures showing the sensitivity of R_{tot} and f_{ac}. The following observations can be made.

1) There is an appreciable change in the ground signatures using different values of these parameters. However, the differences in the loudness metrics are relatively small.
2) This is not meant to be a rigorous study on the impact of these parameters, but based on the two additional cases run, the effect of the characteristic frequency is smaller compared to the impact of radius of curvature. The primary reason for this is that the delta ray conditions are different, leading to differences in the incoming waveform.

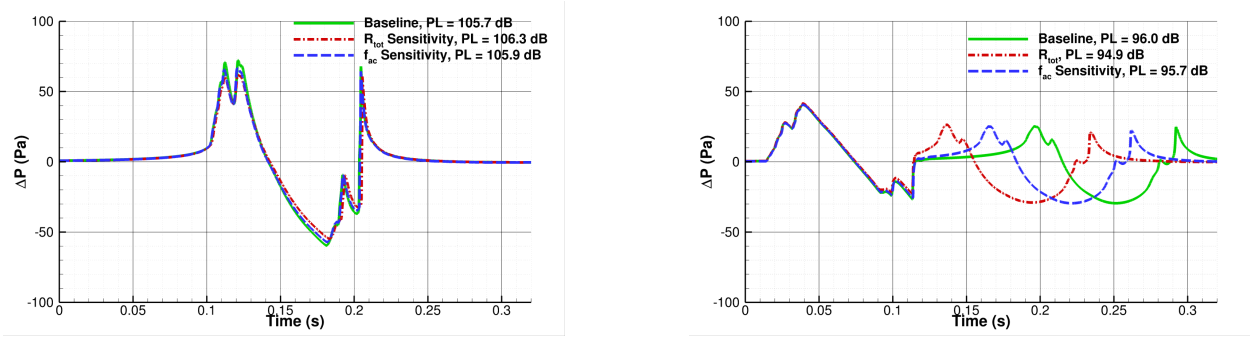

(a) $\overline{Z}$ = **0.05** (b) $\overline{Z}$ = **1.0**

Fig. 10 Post-focus ground signature sensitivity at azimuthal angle = $0°$**.**

3) Under the assumption $R_{tot} \approx R_{cau} \approx 57,921$, $\overline{Z} \approx 0.0385$ to be at the same physical location corresponding to a value of $\overline{Z} = 0.05$ for the other two cases. Although the captions in Figs. 10(a) and 10(b) specify a $\overline{Z}$ value, the correct values should be taken from Table 1.
4) The biggest impact is on the reflected post-focus signature at $\overline{Z} = 1$, where the reflected wave is much closer to the incoming waveform when $R_{tot} \approx R_{cau}$.

C. Case 2: C609

As in the previous case, the given near-field pressures are propagated to the ground to first determine lateral cut-off azimuthal angles, which were computed to be $-63.8°$ and $70.7°$. These angles are much larger than those under standard atmospheric conditions ($\pm 44.8°$). This translates to an increase in primary carpet width of about 28.17 nautical miles for positive azimuthal angles and about 14.03 nautical miles for negative azimuthal angles compared to the standard atmospheric propagation. Figure 11(a) depicts the ground signatures computed at some selected azimuthal angles, while Fig. 11(b) depicts the ground signatures for the same case assuming a standard atmosphere. Standard atmospheric propagations have higher pressure magnitudes compared to the required non-standard atmosphere. The primary observations from Fig. 11(a) are the same from Fig. 3. One noticeable difference is that in this case ground signatures on the positive azimuths are slightly larger than their negative azimuth counterparts, whereas this is reverse for the C25P case. For the sake of completeness, the loudness carpet for this case is depicted in Fig. 12, where the loudness metrics are listed for both the windy atmosphere as well as the standard atmosphere. The primary take-away is that the standard atmosphere carpet is smaller compared to the non-standard atmosphere. Another observation is that the loudness level is fairly flat for most of the inner carpet for both the C25P and C609 cases, demonstrating that both designs are well balanced and optimized for the entirety of the carpet rather than being point designs minimizing sonic boom along the flight track at the detriment of outer azimuthal angles.

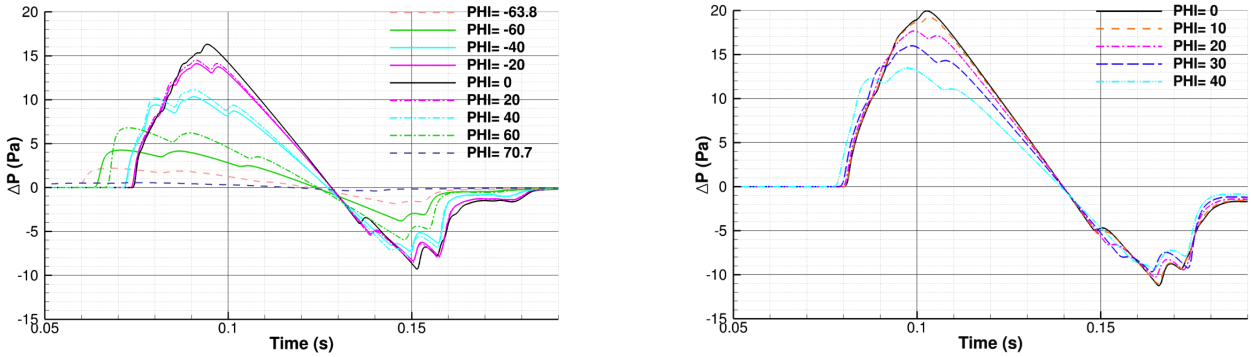

(a) **C609 Ground Signatures: Non-Standard Atmosphere** (b) **C609 Ground Signatures: Standard Atmosphere**

Fig. 11 Case 2 ground signatures.

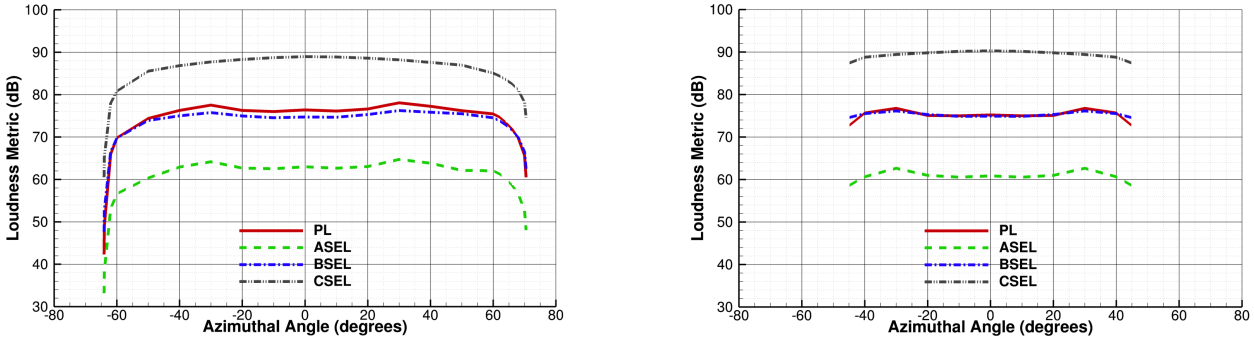

(a) **C609 Loudness Carpet: Non-Standard Atmosphere**

(b) **C609 Loudness Carpet: Standard Atmosphere**

Fig. 12 Case 2 sonic boom loudness carpets.

sBOOM has some unique features that are very useful to aircraft designers and the next few paragraphs showcase some of these as applied to the Case 2. Loudness build-up plots, as depicted in Fig. 13 for some selected azimuthal angles, are used to depict a cumulative effect of loudness on the ground signature. The majority of the loudness build-up occurs either in the shock pressure rise in the front portion or in the aft shock system. A reverse loudness build-up is the same as the forward build-up except the loudness is summed starting at a downstream location where the pressure has reached ambient values. These plots determine whether the loudness is dominated by the front shock system or the aft shock system. Figures 13(a) through 13(c) show that the loudness distribution is well balanced with a slight skew toward the aft shock system, whereas Fig. 13(d) shows that at higher azimuthal angles the front shock system dominates the overall loudness of the ground signature. This feedback could be used by the designer to achieve concept designs with loudness profiles that are appropriately front and aft balanced across the entire boom carpet.

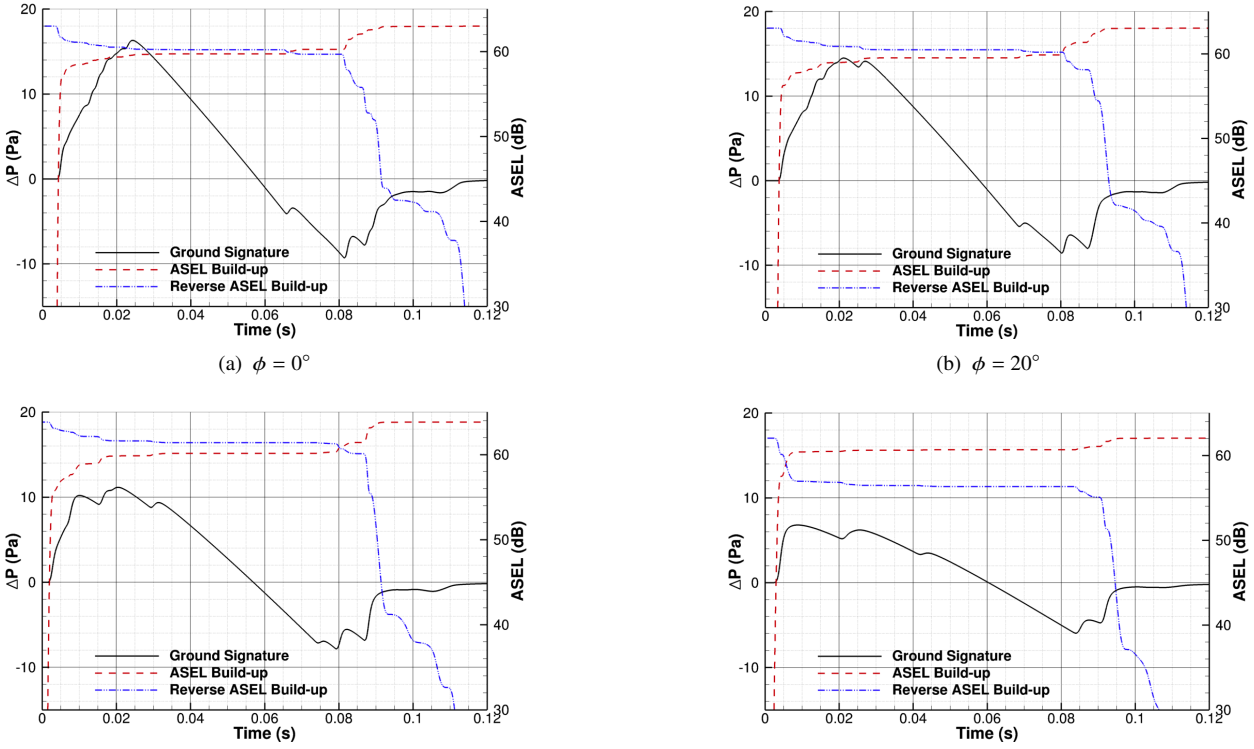

(a) $\phi = 0°$

(b) $\phi = 20°$

(c) $\phi = 40°$

(d) $\phi = 60°$

Fig. 13 Case 2 loudness build-up plots.

The next comparisons pertain to the numerical procedure by which the nonlinearities in the augmented Burgers equation are solved. The default procedure for solving nonlinearities in sBOOM is the Poisson solution [10] of the pressures on the distorted grid with re-interpolation back to the original uniform mesh. However, past research [23] applied the Poisson solution method to the acoustic potential, rather than directly on the pressures. Using the acoustic potential method, multi-valuedness need not be explicitly avoided because the positions of shocks are automatically determined as the intersections of the several branches of the multi-valued acoustic potential Poisson solution. Therefore, instead of dynamically reducing the step size to avoid multi-valuedness in the pressure signature, potentially larger steps can be taken in the solution of the nonlinearity. This method has been implemented in sBOOM and Fig. 14 depicts the results for Case 2 at some selected azimuthal angles, comparing this against the default Poisson pressure solution implementation. Figure 14(a) shows the Poisson and Acoustic Potential (AP) solutions for the windy atmosphere as well as for the standard atmosphere. Although both methods lead to almost identical results in the absence of winds, significantly different ground signatures are observed in the presence of winds. This shows that seemingly insignificant approximations in the numerical solution process can have a large cumulative impact over large distances, particularly in the case of shaped sonic boom signatures with low loudness values. Therefore, one needs to pay close attention to the numerical error build-up in the sonic boom prediction process and ensure that the results can still be trusted with some confidence bounds. This result leads us into the final topic of this paper which is discussed next.

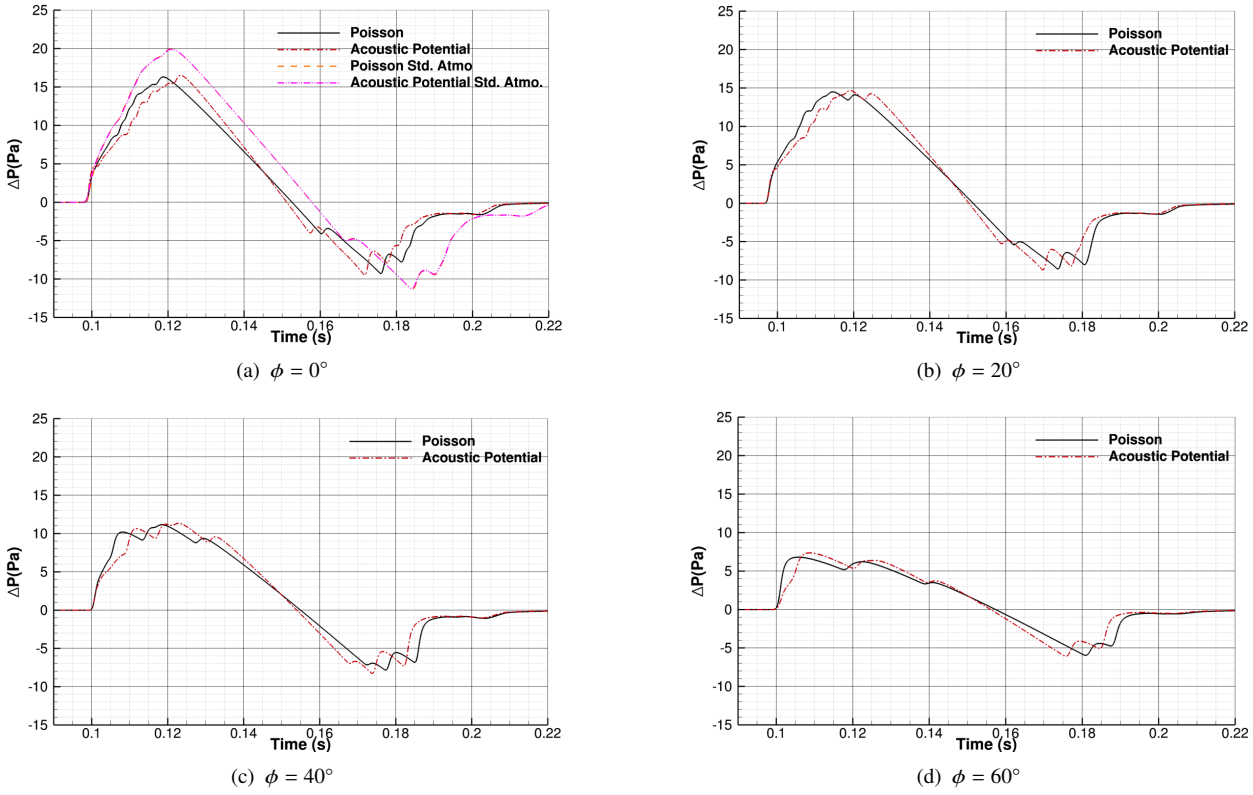

(a) $\phi = 0°$ (b) $\phi = 20°$

(c) $\phi = 40°$ (d) $\phi = 60°$

Fig. 14 Case 2 Poisson solution versus Acoustic Potential implementation of nonlinearity.

As with any numerical model, the predictions are only as good as the inherent assumptions as well as several other implementation specific parameters. One of the ways to assess the error is to obtain asymptotic error estimates or predictions of sonic boom ground signatures as the sampling frequency increases. To determine the asymptotic error behavior, the Richardson extrapolation technique, as implemented and developed by the Cart3D group [24], is exercised for Case 2 of the workshop. This technique predicts regions of low and high confidence in the ground signatures as the sampling frequency used during atmospheric propagation gradually increases. Based on Fig. 15, the front portion of the ground signatures are fully converged, whereas the aft portion of the signatures may be predicted with high confidence to lie within the bounds shown based on the trends observed in coarse, medium, and fine meshes, which correspond to sampling frequencies of 200, 400, and 800 KHz, respectively.

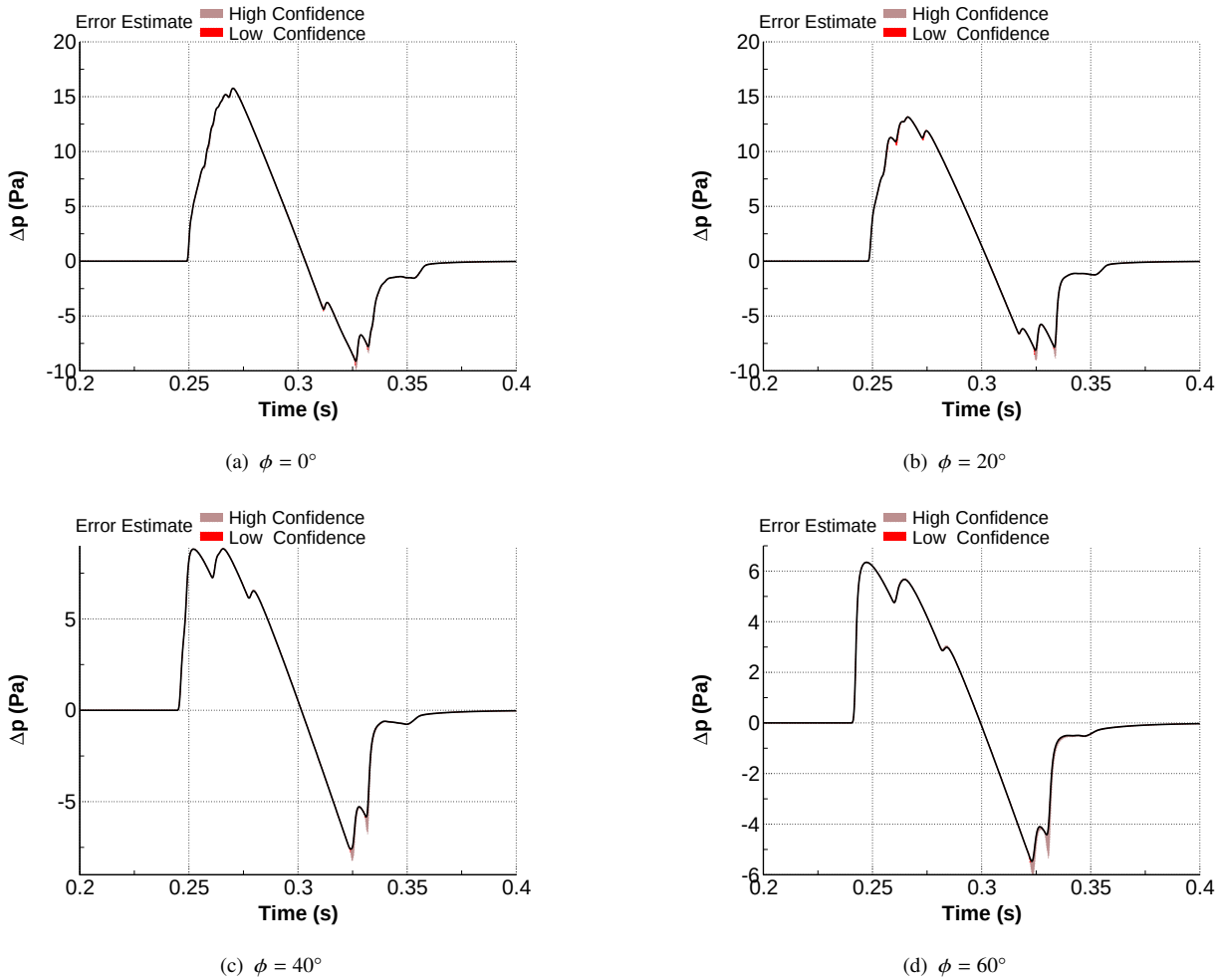

(a) $\phi = 0°$

(b) $\phi = 20°$

(c) $\phi = 40°$

(d) $\phi = 60°$

Fig. 15 Case 2 asymptotic error estimates of ground signatures.

VI. Conclusions

The cases of the 3rd Sonic Boom Prediction Workshop (SBPW3) were propagated using sBOOM. All the required and optional cases were analyzed and presented with detailed discussion. Some unique features and results associated with sBOOM were presented and discussed.

The main conclusions based on this study are:

1) Realistic sonic boom primary carpets could potentially be larger than those predicted with standard atmospheric conditions.
2) BSEL and PL loudness metric magnitudes are very close to each other.
3) Focus boom predictions are sensitive to focusing geometry and characteristic frequency. Care must to be taken to ensure that the interfacing between Burgers and LNTE domains is properly handled. Otherwise, the results could be erroneous.
4) Loudness build-up plots provide quick insight and actionable feedback for aircraft designers to focus their efforts on appropriate regions of the Outer Mold Line (OML).
5) As the sonic boom loudness levels get lower, special attention has to be given to the error inherent in the propagation mechanisms and the numerical implementation of these underlying processes.
6) Asymptotic error estimates offer one way to obtain confidence bounds on the sonic boom ground signatures.

Acknowledgments

The author wishes to thank NASA's Commercial Supersonic Technology (CST) project for sponsoring this research and supporting the 3rd Sonic Boom Prediction Workshop (SBPW3). Many thanks to Joseph Salamone and the entire NASA SCAMP team in developing and validating the LNTE solver. Thanks also to Masashi Kanamori (JAXA), Juliet Page (Volpe) and Sophie Kaye (Volpe) for collaborating and taking the time to discuss the optional focus boom computational domain set-up. The author also gratefully acknowledges support from the Cart3D team in determining the asymptotic error estimates. Help from SBPW3 organizers (Melissa Carter, Michael Park, Alaa Elmiligui) and participants in various forms is also much appreciated.

References

[1] Park, M. A., and Morgenstern, J. M., "Summary and Statistical Analysis of the First AIAA Sonic Boom Prediction Workshop," *AIAA Journal of Aircraft*, Vol. 53, No. 2, 2016, pp. 578–598. doi:10.2514/1.C033449.

[2] Park, M. A., and Nemec, M., "Near Field Summary and Statistical Analysis of the Second AIAA Sonic Boom Prediction Workshop," *AIAA Journal of Aircraft*, Vol. 56, No. 3, 2019, pp. 851–875. doi:10.2514/1.C034866.

[3] Rallabhandi, S. K., and Loubeau, A., "Summary of Propagation Cases of the Second AIAA Sonic Boom Prediction Workshop," *AIAA Journal of Aircraft*, Vol. 56, No. 3, 2019, pp. 876–895. doi:10.2514/1.C034805.

[4] Rallabhandi, S. K., "Advanced Sonic Boom Prediction Using the Augmented Burgers Equation," *AIAA Journal of Aircraft*, Vol. 48, No. 4, 2011, pp. 1245–1253. doi:10.2514/1.C031248.

[5] Pierce, A. D., *Acoustics: An Introduction to Its Physical Principles and Applications*, Acoustical Society of America, 1989.

[6] Lonzaga, J. B., "Recent Enhancements to NASA's PCBoom Sonic Boom Propagation Code," AIAA 2019-3386, 2019.

[7] Hayes, W. D., Haefeli, R. C., and Kulsrud, H. E., "Sonic Boom Propagation in a Stratified Atmosphere with Computer Program," Tech. Rep. NASA CR-1299, Aeronautical research associates of Princeton Inc., Princeton,NJ, Apr. 1969.

[8] Hamilton, M., and Blackstock, D., *Nonlinear Acoustics*, Academic Press, 1998. URL `https://books.google.com/books?id=k-kWozCE0jIC`.

[9] Robinson, L. D., "Sonic Boom Propagation Through an Inhomogeneous Windy Atmosphere," Ph.D. thesis, University of Texas at Austin, 1991.

[10] Cleveland, R. O., "Propagation of Sonic Booms Through a Real, Stratified Atmosphere," Ph.D. thesis, University of Texas at Austin, 1995.

[11] Lee, Y.-S., and Hamilton, M. F., "Time-domain Modeling of Pulsed Finite-amplitude Sound Beams," *The Journal of the Acoustical Society of America*, Vol. 97, No. 2, 1995, pp. 906–917. doi:10.1121/1.412135.

[12] Rallabhandi, S. K., Nielsen, E. J., and Diskin, B., "Sonic Boom Mitigation Through Aircraft Design and Adjoint Methodology," *AIAA Journal of Aircraft*, Vol. 51, No. 2, 2014. doi:10.2514/1.C032189.

[13] Stevens, S., "Perceived Level of Noise by Mark VII and Decibels(E)," *Journal of the Acoustical Society of America*, Vol. 51, No. 2, 1972, pp. 575–601.

[14] Leatherwood, J. D., Sullivan, B. M., Shepherd, K. P., McCurdy, D. A., and Brown, S. A., "Summary of Recent NASA Studies of Human Response to Sonic Booms," *The Journal of the Acoustical Society of America*, Vol. 111, No. 1, 2002, pp. 586–598. doi:10.1121/1.1371767.

[15] Loubeau, A., Naka, Y., Cook, B. G., Sparrow, V. W., and Morgenstern, J. M., "A New Evaluation of Noise Metrics for Sonic Booms Using Existing Data," *2nd International Sonic Boom Forum*, 20th International Symposium on Nonlinear Acoustics, 2015.

[16] NASA, "Low-Boom Flight Demonstrator Project," `https://www.nasa.gov/aeroresearch/programs/iasp/lbfd`, 2020. Online; accessed 20 May 2020.

[17] Rallabhandi, S. K., and Loubeau, A., "Summary of Propagation Cases of the Third AIAA Sonic Boom Prediction Workshop," AIAA SciTech 2021 American Institute of Aeronautics and Astronautics, Reston, VA (submitted for publication).

[18] Page, J. A., Plotkin, K., Hobbs, C., Sparrow, V., Salamone, J., Cowart, R., Elmer, K., Welge, H. R., Ladd, J., Maglieri, D., and Piacsek, A., "Superboom Caustic Analysis and Measurement Program (SCAMP) Final Report," NASA CR-2015-218871, Langley Research Center, Aug. 2015. doi:2060/20150019419.

[19] Auger, T., and Coulouvrat, F., "Numerical Simulation of Sonic Boom Focusing," *AIAA Journal*, Vol. 40, No. 9, 2002, pp. 1726–1734.

[20] Kandil, O., and Zheng, X., "Prediction of Superboom Problem using Computational Solution of Nonlinear Tricomi Equation," AIAA Paper 2005–6335, 2005.

[21] Salamone, J. A., "Solution of the Lossy Nonlinear Tricomi Equation with Application to Sonic Boom Focusing," Ph.D. thesis, The Pennsylvania State University, 2013.

[22] Salamone, J. A., Sparrow, V. W., and Plotkin, K. J., "Solution of the Lossy Nonlinear Tricomi Equation Applied to Sonic Boom Focusing," *AIAA Journal*, Vol. 51, No. 7, 2013. doi:10.2514/1.J0052171.

[23] Marchiano, R., Coulouvrat, F., and Grenon, R., "Numerical Simulation of Shock Wave Focusing at Fold Caustics, with Application to Sonic Boom," *The Journal of the Acoustical Society of America*, Vol. 114, No. 4, 2003, pp. 1758–1771. doi:10.1121/1.1610459.

[24] Anderson, G. R., Aftosmis, M. J., and Nemec, M., "Cart3D Simulations for the Second AIAA Sonic Boom Prediction Workshop," *AIAA Journal of Aircraft*, Vol. 56, No. 3, 2017, pp. 896–911. doi:10.2514/1.C034842.